Contaminants in Aquatic and Terrestrial Environments

Biomass-derived provenance dominates glacial surface organic carbon in the western Himalaya

Sarwar Nizam, Indra Sekhar Sen, V. Vinoj, Valier Galy, David Selby, Mohammad F. Azam, Satyendra Kumar Pandey, Robert A. Creaser, Avinash Kumar Agarwal, Akhilendra Pratap Singh, and Michael Bizimis

Environ. Sci. Technol., **Just Accepted Manuscript** • DOI: 10.1021/acs.est.0c02710 • Publication Date (Web): 25 Jun 2020

Biomass-derived provenance dominates glacial surface organic carbon in the western Himalaya

SARWAR NIZAM[1]*, INDRA S.SEN[1], VELU VINOJ[2] , VALIER GALY[3], DAVID SELBY[4,5], MOHAMMAD F. AZAM[6],SATYENDRA K. PANDEY[2], ROBERT A. CREASER[7], AVINASH K. AGARWAL[8], AKHILENDRA P. SINGH[8], MICHAEL BIZIMIS[9]

[1]Department of Earth Sciences, Indian Institute of Technology Kanpur, Kanpur, UP 208016, India.

[2]School of Earth, Ocean and Climate Sciences, Indian Institute of Technology Bhubaneswar, Odisha, 752050, India.

[3]Department of Marine Chemistry and Geochemistry, Woods Hole Oceanographic Institution (WHOI), 266 Woods Hole Road, Woods Hole, MA 02543, USA.

[4]Department of Earth Sciences, University of Durham, Durham DH1 3LE, UK.

[5]State Key Laboratory of Geological Processes and Mineral Resources, School of Earth Resources, China

[6]Discipline of Civil Engineering, School of Engineering, Indian Institute of Technology Indore, Indore 453552, India.

[7]Department of Earth & Atmospheric Sciences University of Alberta, 126 ESB Edmonton Alberta Canada T6G2R3.

[8]Engine Research Laboratory, Department of Mechanical Engineering, Indian Institute of Technology Kanpur, UP, 208016, India.

[9]School of Earth, Ocean and Environment, University of South Carolina, Columbia, SC 29208, USA.

**Correspondence to: sarwar@iitk.ac.in*

Abstract

The origin, transport pathways, and spatial variability of total organic carbon (OC)on the western Himalayan glaciers is poorly understood compared to that of black carbon (BC) and dust, but it is critically important to evaluate the climatic role of OC in the region. Applying the distribution of OC activation energy, ^{14}C activity and radiogenic isotopes of $^{208}Pb/^{204}Pb$, $^{207}Pb/^{204}Pb$ and $^{206}Pb/^{204}Pb$ in glacial debris and atmospheric particulate matter (PM_{10} size fraction) we demonstrate that 98.3± 1.6% and 1.7± 1.6% of the OC in western Himalayan glaciers are derived from biomass and petrogenic sources, respectively. The $\delta^{13}C$ and N/C composition shows that the biomass is a complex mixture of C3 vegetation and autochthonous photo-autotrophic inputs modified by heterotrophic microbial activity. The dataset reveals that the studied western Himalayan glacier has negligible contributions from fossil fuel derived particles, which contrasts to the central and eastern Himalayan glaciers that have significant contributions from fossil fuel sources. We show that this spatial variability of OC sources relates to regional differences in air-mass transport pathways and precipitation regimes over the Himalaya. Moreover, our observation suggests that biomass-derived carbon could be the only primary driver of carbon-induced glacier melting in the western Himalaya.

1. Introduction

Worldwide glaciers are losing mass at an average rate of 0.48± 0.20 meter water-equivalent per year (m w.e. yr^{-1})[1], with the rate of Himalayan glacier mass wastage nearly doubling (−0.43± 0.14 m w.e.yr^{-1}) in recent years.[2] This accelerated mass loss is considered to be primarily related to the well-established long-term increase of the Earth's near surface temperature and anthropogenic climate change.[3,4] In addition to this warming, the reduction of surface ice albedo by ice surface deposits of dark colored impurities constitutes an additional control of glacier melting rate.[5–7] Impurities that darken the ice surface and directly increase the heat absorption and thus enhance ice melting comprise dust, BC (black carbon, e.g., soot), and other forms of OC not derived from combustion.[8–11] In this study, OC refers to the total organic carbon that comprises the entire pool of organic carbon including both organic and elemental carbon. Further, we classify the OC as OC_{ff} (fossil fuel) and OC_{bio} (biomass) referring to OC derived from either fossil fuel or biomass sources, such as biomass burning derived particles, atmospheric organic matters, and glacial microbes.[5]

The contribution to glacier surface darkening by particle matter and its attendant impact on glacial melt across high Asian mountain glaciers is variable. For example, the main contributor to glacier surface warming in Eastern Himalaya and Central Asia is BC, while mineral dust is a dominant factor in the western Himalaya.[12] As a result, previous studies have mainly focused on BC and dust, owing to their greater heat absorption capacities.[13–16] Heretofore, limited research on total OC has led to substantial uncertainties and incomplete knowledge of the impact of OC in the Himalaya and Tibetan Plateau.[17–19] Thus, given the almost 20% albedo reduction related to OC for glaciers in Asia[12], a thorough assessment of the origin, transport pathways, and spatial distribution of OC is paramount to reduce the uncertainties in

estimating the impact of carbon on the rate of glacial melting of Himalayan glaciers. In addition to the albedo effect of light absorbing impurities, carbonaceous aerosols also warm up the air mass over glaciers, and support microbial life[22], both of which further contributes to enhanced rates of glacier melting. It is also noteworthy that algal or microbial communities on the glacier surface act as a sink for carbon and other impurities, and may yield a greater positive feedback on glacier melting when compared to OC_{ff}.[23]. As such, constraints on the composition of OC will help better quantify the future impact of increasing anthropogenic emission surrounding Himalayan glaciers (Figure S1), and its attendant controls on the hydrological regimes of glacier-sourced large river systems such as the Indus, Ganges, and Brahmaputra. The findings will also aid in quantifying the contribution of Himalayan glaciers melt to eustatic sea-level rise[1], currently estimated to raise sea level by 0.52 cm by the end of 21st century.[24]

In contrast to model-based approaches[26-28], recent radiocarbon measurements on BC particles deposited on glaciers and in aerosols revealed a much higher (~50%) fossil fuel contribution across the Himalayan-Tibetan Plateau.[25] These radiocarbon measurements were however restricted to the central and eastern Himalayan region, which falls under the strong influence of the Indian Summer Monsoon. Further, the eastern and western areas of the Himalayan region have different climatology, hydrology, meteorology, as well as glacier behavior and dynamics.[29–31] The large geographical spread (~2500 km) of the Himalaya over different climate regimes makes it very difficult to extend the findings of one climate regime to the other. Moreover, in-situ OC measurements of glacier and snow samples in the western Himalaya including Hindu-Kush and Karakoram region are not available, despite the fact that the western region holds >70% of the total ice mass of the Himalaya.[32] With one-sixth of the world's population dependent on the Himalayan glacier meltwater and the increase in anthropogenic

emissions in the Indian subcontinent (Figure S1), understanding the origin and transport pathways of OC on the western Himalayan glaciers and its impact on glacier melting rate is an issue of global significance.

To understand the origin, transport pathways and spatial variability of OC on the western Himalayan glaciers, this study focuses on the source area and origin of dust and OC on the ablation zone (>4500 m a.s.l.) of the Chhota Shigri Glacier (CSG, 32.2° N, 77.5° E) in the Lahaul-Spiti valley of the western Himalaya, India (Figure 1). Cryoconite and supra-glacial moraine sediments from the CSG surface were investigated to characterize the origin of carbonaceous particles. Cryoconites are small water filled depressions containing a dark colored mixture of dust, OC, BC, and microbes collected over several years. Further, to constrain the source end-members, atmospheric particulate matter (PM_{10}) were collected in Harsil (31.1° N; 78.7° E; 2634 m a.s.l.) and Kanpur (26.1° N; 80.2° E).The Harsil site is located in a high altitude remote Himalayan forested area that records a history of major forest fires (Figure S3). Harsil is >125 km from major urban settlements and industrial activities, thus the collected aerosol at Harsil serves as the best proxy for the OC_{bio} and pristine Himalayan end-member. To obtain the best estimate of OC_{ff} aerosol, a sample was collected from ~5 Km north of a coal-fired thermal power plant (Panki Thermal Power Plant) and a kilometer west of a National Highway (NH91) in Kanpur –one of the largest industrialized centers in the Indo-Gangetic plain (Figure 1). Analysis of samples followed a multi-disciplinary approach, coupling organic and inorganic geochemical tracers including Ramped Pyrolysis Oxidation (RPO), ^{14}C activity, $\delta^{13}C$, $^{208}Pb/^{204}Pb$, $^{207}Pb/^{204}Pb$, $^{206}Pb/^{204}Pb$, TOC, N, and heavy metal concentrations with Hybrid Single Particle Lagrangian Integrated Trajectory Model (HYSPLIT) air mass trajectory modeling was used to determine OC origin and transport pathways identification.

2. Materials and Methods

2.1 Sampling details

Cryoconite debris was collected from 20 sites in the ablation zone (4515 - 4928 m a.s.l.) of the CSG during July, 2017. In addition to cryoconite, 5 moraine debris samples were also collected. The samples were first dried on a hot plate at ~70 °C to remove the moisture content. Moraine debris samples were sieved to get bulk (DB <3 mm) and particulate (<63 μm: DF) fraction for geochemical analysis. Bulk cryoconite and moraine debris samples (DB and DF) were ground to a homogeneous powder (20μm size) in an agate mil for further chemical analysis. Atmospheric particulate matter (PM_{10} size fraction) sampling in Kanpur and Harsil were carried out using high-volume (1000 L/min) atmospheric aerosol samplers (Envirotech PM_{10} sampler, model APM 460 DXNL). In Kanpur and Harsil, PM_{10} sampler was operated for 24 (on January 1, 2016) and 48 hours (April 12 to April 14, 2016), respectively. Detailed sampling protocol description is outlined in Nizam and Sen, 2018.[33]

2.2 Ramped Pyrolysis Oxidation (RPO), ^{14}C ages, bulk $\delta^{13}C$, N and C analysis

The RPO analysis was carried out at the National Ocean Sciences Accelerator Mass Spectrometer facility (NOSAMS, Woods Hole Oceanographic Institution). The RPO instrument involves continuous sample heating, with the CO_2 evolved being trapped for dual C-isotope analysis. Importantly, RPO analyzes 100% of the OC in the sample, irrespective of the nature of the OC. Two cryoconite (C9 and C14), one moraine (DF6), and two aerosol samples were selected for RPO analysis. The instrumental makeup and analytical protocol adopted for RPO analysis has been described in detail in previous studies.[34,35] Briefly, 30–70 mg powder sample aliquots were loaded into a pre-combusted (at 850 °C for 5 hours) quartz reactor, heated at a 5 °C min^{-1} ramp rate in a two-stage oven. This incremental heating leads to the release of CO_2, which was cryogenically purified, trapped and flame sealed into a glass tube containing nuggets of Ag

(~10 mg) and CuO (~100 mg). The CO_2 concentration in the carrier gas (in parts per million by volume, ppm CO_2) is continuously measured at a resolution of 1 second by an infrared gas analyzer. CO_2 collected at user-defined temperature intervals is referred to as RPO fractions. Each RPO fraction collected is graphitized with the radiocarbon abundance determined via Accelerated Mass Spectrometry at NOSAMS and reported as fraction modern (F_m). Meanwhile, a 10% split of each RPO fraction was used for stable isotopes ($\delta^{13}C$) analysis using a dual-inlet Isotope Ratio Mass Spectrometer (IRMS).

The $\delta^{13}C$ values are expressed in part per mill (‰) notation relative to Vienna Pee Dee Belemnite (VPDB). The F_m and $\delta^{13}C$ ratios of the RPO fractions are reported in Table 1. In addition, bulk $\delta^{13}C$, total organic carbon (OC), total nitrogen (N) were also measured in all of the cryoconite and selected moraine samples using IRMS at Woods Hole Oceanographic Institution (Table S1). The bulk $\delta^{13}C$ value calculated as the mass weighted average of all RPO fractions showed good agreement with the measured bulk $\delta^{13}C$ value, with the exception of moraine sample DF6. The mismatch appears to be driven by the high $\delta^{13}C$ value of the first RPO fraction collected for this sample. We inferred this enriched stable isotope composition is related to some technical error during IRMS analysis. The results for all of the RPO (and IRMS) analyses were blank and kinetic isotope fractionation corrected.[36] Corrected data was used to calculate the activation energy distribution using the rampedpyrox python package[37], which has been described in detail in previous studies.[35] Radiocarbon age (in ^{14}C yr BP) was calculated using corrected Fm values and the Libby half-life as: age = -8033 ln (F_m).

2.3 Lead isotope analysis

Ten cryoconite and two moraine samples (DF) were selected for Pb isotopes analysis. The Pb isotopic data was obtained from the Radiogenic Isotope Facility from the Department of

Earth and Atmospheric Sciences at the University of Alberta. Approximately 4-12 mg of sample powder (depending on lead abundance), was dissolved in ultrapure HF/HNO_3 at 100°C for 2 days. Sample solutions were then evaporated under ULPA-filtered air and converted to chlorides using 6N HCl, then bromides using 2N HBr. The Pb was purified by standard anion exchange chromatography using HBr and HCl as eluents under ULPA-filtered conditions. The isotopic composition of Pb then measured by Nu Plasma MC-ICPMS in static analysis mode. The measured Pb isotope ratios were corrected for instrumental mass bias using the agreed value for $^{203}Tl/^{205}Tl$ ratio measured simultaneously with each Pb analysis.[38] Overall reproducibility of any Pb isotope measurement is based on >6 years of analyses of SRM981 Pb isotope standard. At the first uncertainty level, the reproducibility of the SRM981 measured isotopic ratios are: $^{206}Pb/^{204}Pb$ = 0.016%; $^{207}Pb/^{204}Pb$ = 0.018%; $^{208}Pb/^{204}Pb$ = 0.018%. The most widely accepted values for this Pb isotope standard are those determined by double-spiked TIMS analysis in previous study[39], which are: $^{206}Pb/^{204}Pb$ = 16.936; $^{207}Pb/^{204}Pb$ = 15.489; $^{208}Pb/^{204}Pb$ = 36.701. The absolute values of Pb isotope ratios for SRM981 determined during the course of the analyses report here are: $^{206}Pb/^{204}Pb$ = 16.936; $^{207}Pb/^{204}Pb$ = 15.488; $^{208}Pb/^{204}Pb$ = 36.690. The Pb isotope ratios are reported in Table 2.

2.4 Heavy metal analysis

Heavy metal concentration analyses were performed in Indian Institute of Technology Kanpur on a Quadrupole Inductively Coupled Plasma Mass Spectrometer (ThermoFisher Scientific, Q-ICP-MS) system. Briefly, approximately 25 mg of sample powder was digested using a mixture of HF (3 parts) and HNO_3 (1 part) for. Six procedural blanks, Reference Material SBC-1 (Shale) from US Geological Survey (USGS) were also digested following the same procedures. The final concentrations were blank corrected using the average procedural blank

concentrations and matrix effect was corrected by In normalization (Table S1). Average blank corrections were less than 1% for most of the elements. The measured Sc, V, Cr, Ni, Cu, Zn and Pb concentration of SBC-1 were 20± 1, 205± 3, 101± 2, 81± 1, 30± 0.2, 191± 2 and 33± 1 (1 SD, n = 6), respectively, which is in close agreement with the USGS certified values of 20± 0.2, 220± 1.4, 109± 1, 83± 0.8, 31± 0.6, 186± 2 and 35± 0.3, respectively.

2.5 Air Mass Back Trajectory Analysis

Hybrid Single Particle Lagrangian Integrated Trajectory Model (HYSPLIT) modeling was used to compute the air parcel back trajectories for every hour for five different sites that includes Leh, ChhotaShigri, Thorong, Qiangyong, and Yulong sites for the year 2016 (Figure 1). The archived meteorological analysis from National Centers for Environmental Prediction (NCEP) Global Data Assimilation System (GDAS) model was used to estimate the trajectories. Annual as well as seasonal trajectory analysis was carried out to elucidate the major source regions of air mass reaching the Himalaya (Figure 1 and Figure S2). A total of 24x365 or 8760 trajectory pairs were simulated for each of the sites. A density map was created at a resolution of 0.25^{o} x 0.25^{o} resolution to obtain fraction of total trajectories passing through each of the grid cell. This provided an indication of the percentage or probability of influence of each grid point to the air mass reaching the receptor site. Two contour intervals of 0.1 and 0.5 that represented 10 and 50% trajectories passing through any grid was created for each site.

3. Results and Discussion

The distribution of OC activation energy (Ea), $\delta^{13}C$, and ^{14}C content (expressed as fraction modern, Fm) for cryoconite, moraine sediments (particulate fraction) and PM_{10} were compared to fingerprint the sources of OC (Figure 2). Activation energy is a proxy for OC reactivity, and each OC pool has a distinct Ea distribution reflecting its overall bonding

environment (e.g. molecular composition, association with mineral surfaces).[35] Using Ea, $\delta^{13}C$ and ^{14}C ages, it is thus possible to fingerprint the sources of OC. For example, biomass-derived OC have lower Ea (<150 kJ mol^{-1}), high Fm (~1.0), and modern ages, whereas fossil-derived OC possess higher Ea (>150 kJ mol^{-1}) and Fm = 0.[40] Among the fossil sources, OC derived from Himalayan petrogenic sources (OC_{petro}) has a much higher Ea (≥200 kJ mol^{-1},) than fossil fuel derived OC (OC_{ff} < 200 kJ mol^{-1}).[40,41]

The PM_{10} collected at Harsil and Kanpur has distinct Ea distributions and ^{14}C compositions (Table 1, Figure 2). The Ea distributions of Harsil and Kanpur PM_{10} OC show a predominant peak at ca. 135 and 165 kJ mol^{-1}, respectively. The Harsil PM_{10} OC is also characterized by young ^{14}C ages (RPO Fm values >0.94; bulk Fm = 0.99). A predominant Ea peak at ca. 135 kJ mol^{-1} and young ^{14}C ages of Harsil PM_{10} OC clearly corresponds to OC_{bio}.[40] It is possible that some of the particles could contain soil organic carbon (SOC). However, SOC is expected to be pre-aged, as observed in mineral soils globally and suspended sediments of Himalayan sourced rivers.[42,43] Further, dust contributions from arid areas (e.g., Thar Desert) would similarly be expected to carry an old ^{14}C signature owing to conditions promoting organic matter preservation. Our data is not consistent with SOC inputs as it shows a flat, near-modern ^{14}C ages across the Ea spectrum. In contrast, Kanpur PM_{10} OC is characterized by lower Fm values (0.4<Fm<0.8; bulk Fm = 0.64) and corresponding older ^{14}C ages. A predominant Ea peak at ca. 165 kJ mol^{-1} and older ^{14}C ages of Kanpur PM_{10} OC reveal significant contributions from a fossil fuel source. The lower Ea peak in Kanpur PM_{10} OC (ca. 135 kJ mol^{-1}) also points towards some OC_{bio} contribution. A simple binary mixing calculation revealed that the Kanpur PM_{10} OC is composed of ca. 36% OC_{ff} and 64% OC_{bio}. The PM_{10} RPO data further suggest that OC_{bio} and

OC_{ff} have overlapping Ea distributions, although OC_{ff} is more heavily concentrated at higher Ea values.

OC in cryoconite and moraine sediment have similar Ea distributions with peak reactivity between ca. 125 kJ mol^{-1} and 150 kJ mol^{-1}. The low Ea and high Fm values, and modern ^{14}C ages support that OC in these RPO fractions is derived from recently fixed OC sources (OC_{bio}, Fm~1, modern age) such as biomass burning, autochthonous photoautotrophic biomass and heterotrophic microorganisms. Overall, the Ea and ^{14}C signature of cryoconite and moraine sediments are similar to Harsil PM_{10}, confirming an overwhelmingly dominant OC_{bio} input to both cryoconite and moraine sediments. A small portion of cryoconite and moraine OC is characterized by high Ea (>180 kJ mol^{-1}) and low Fm values (older ^{14}C ages). The presence of aged OC exclusively at high Ea values however precludes OC_{ff} as a source, because Kanpur PM_{10} RPO data show that OC_{ff} is distributed over the entire Ea spectrum. Instead, we argue that the high Ea RPO fractions contain a mixture of biomass and petrogenic (rock-derived, OC_{petro}) OC. Indeed, OC_{petro} has been shown to be characterized by high Ea (i.e. >200 kJ mol^{-1}) and Fm values equal to 0.[40] A mass balance approach assuming a binary mixing of ^{14}C dead OC and biomass-derived OC with a ^{14}C age equal to that of Harsil PM_{10}, shows that 1.7± 1.6% of OC in cryoconite and moraine sediment is derived from ^{14}C-dead sources. This proportion translates into a C concentration of 0.02± 0.02%. Such a low concentration of ^{14}C-dead OC is consistent with the expected OC_{petro} concentration in the high-grade crystalline rocks of the CSG catchment and Himalayan rocks in general.[44] It is also lower than the average OC content of bulk moraine samples (0.064± 0.020%), which, based on bulk geochemical characterization are dominated by OC_{petro}. We conclude that cryoconite and moraine sediment have negligible OC_{ff} and contain a mixture of OC_{bio} (98.3± 1.6%) and minor OC_{petro} inputs (1.7± 1.6%).

Additionally, we used stable carbon isotopes ($\delta^{13}C$) to further establish the source of OC_{bio} in the cryoconite and moraine sediment. The majority of the cryoconite samples have a distinct $\delta^{13}C$ composition with respect to surrounding moraine sediments, as well as to cryoconite samples from Greenland and the Arctic.[45,46] The $\delta^{13}C$ in cryoconite samples ranges between -24.9 to -18.2‰ (average -21.8± 1.7‰, n=20, 1s.d.), which is higher than for moraine sediments (-22.5 to -26.7‰, average -24.2± 1.3‰, n=10, 1s.d.). In general, carbonaceous aerosol derived from burnt C3 type biomass sources in the Indian subcontinent should have a $\delta^{13}C$ value of ca. -26‰[47], which can exhibit a maximum fractionation up to 0.5‰ due to burning emission effect.[48] Burning induced ^{13}C fractionation of C3 type vegetation is therefore insufficient to explain the observed $\delta^{13}C$ enrichment in cryoconite. Therefore, it can be postulated that cryoconite draws some of its enriched $\delta^{13}C$ signature from additional sources or processes.

The $\delta^{13}C$ enrichment in cryoconite samples can be best explained by contributions from photo-autotrophic and heterotrophic micro-organisms in supraglacial cryoconite that produces enrichment of N and $\delta^{13}C$ values.[22,46] Biomass humification processes could also produce enriched $\delta^{13}C$ values, but the RPO-^{14}C data are incompatible with significant SOC inputs. The N/C vs $\delta^{13}C$ plot (Figure 3A) suggests that cryoconite samples are composed of a mixture of ^{13}C depleted and N-poor organic matter that could correspond to a primary C3-derived OC, with ^{13}C enriched and N-rich organic matter that reflects microbial communities growing in the snow/ice environment. According to the RPO data, the ^{13}C-rich, N-rich component is also enriched in ^{14}C (i.e. it has been fixed recently) and relatively labile, further suggesting it corresponds to microbial biomass and/or algae. However, finer apportionment of the different sources of biospheric OC in cryoconite samples would require compound-specific biomarker data. To summarize, our data suggest that the OC in cryoconite and moraine sediments is a complex

mixture of C3 type biomass and autochthonous photo-autotrophic inputs modified by heterotrophic microbial activity. An overall biomass source signature is also supported by heavy metal ratios (Zn/Pb vs Cu/Pb; Figure 3B), assuming that the metal ratios retained the source signature during transportation and transformation changes.

In addition to carbon systematics and heavy metal concentrations, $^{206}Pb/^{204}Pb$ and $^{208}Pb/^{204}Pb$ were used as additional independent tracer to identify the residues of fossil fuel signature on the CSG. The radiogenic Pb isotopes (Table 2), as well as heavy metal enrichment (these are) factor (Figure S4) also support the absence of a fossil fuel signature in cryoconite and moraine sediment from the CSG. Moreover, the $^{206}Pb/^{204}Pb$, $^{208}Pb/^{204}Pb$ overlap with that of the Himalayan crust (Figure 4). The highly linear correlation between $^{206}Pb/^{204}Pb$ and $^{208}Pb/^{204}Pb$ further implies that these elements are sourced from two dominant endmembers. Mixing calculations using Pb isotope systematically show a negligible anthropogenic contribution (<1%, Figure 4). The triple lead isotope data ($^{207}Pb/^{206}Pb$ versus $^{208}Pb/^{206}Pb$) also supports the absence of anthropogenic pollutant contribution in the studied glacier site (Figure S5). Our results differ from previous findings that the Himalayan glaciers in general receive significant long-range transported dust from Africa, Middle East, and Thar desert, as well as from the Indo-Gangetic plain, India.[49,50]

The OC activation energy distribution, ^{14}C, $\delta^{13}C$, $^{208}Pb/^{204}Pb$, $^{207}Pb/^{204}Pb$ and $^{206}Pb/^{204}Pb$, TOC, N, and heavy metal concentrations, therefore, suggest that the studied western Himalayan glaciers have negligible contribution from OC derived from fossil fuel combustion sources. The difference between our findings and a previous study reporting ~50% fossil fuel sourced carbon contribution in central and eastern Himalayan glaciers[25] can be explained by air mass transport pathways and rainfall intensity. A HYSPLIT air mass trajectory modeling results reveal that the

eastern and central Himalayan glaciers that have received up to half of the BC from fossil fuel sources draw a significant fraction of their air mass from the heavily polluted Indo-Gangetic Plains (IGP) (Figure 1). In contrast, annual and seasonal (Figure 1 and Figure S2) air mass back trajectory modeling at the study site shows that the western Himalayan regions receive limited air-mass transport from the polluted IGP and less rainfall when compared to central and eastern Himalaya, confirming the limited transport of ambient anthropogenic pollutants from the IGP.

The estimated glacial mass loss rates between 2000-2016 in western, central, and eastern Himalaya are similar (-0.40, -0.35, -0.53 m w.e yr^{-1}, respectively).[51] Glacial mass loss rate reported for the CSG (-0.56 m w.e.yr^{-1} between 2002 and 2014)[52] is slightly higher than regional averages. Since glacial mass loss is similar across the Himalaya and CSG is essentially free of OC_{ff}, our observation suggests that OC_{bio} would be the primary driver of carbon-induced glacier melting in the western Himalaya. Direct aerosol measurements studies over the western and northwestern Himalaya hill stations also supports a predominant burnt carbon biomass source.[53,54] Given that it is well known that OC_{ff} particles are more readily transported over long-distances compared to OC_{bio}[55], and thus, if OC_{bio} were transported from geographically distant sources, OC_{ff} particles were expected to be similar or higher in concentration compared to OC_{bio} in western Himalayan glaciers. The near absence of OC_{ff} and prevalence of local air mass circulation therefore indicate that carbonaceous particles in western Himalaya are only derived from locally burnt biomass sources. Thus, given that OC emissions are projected to be 21-28 Tg by 2050[56], leading to new climate policies to curb global carbon emissions in urban centers, considering the impact of local carbonaceous aerosols on glacier mass loss in the western Himalaya is necessary to model the change in the glacial mass of western Himalayan glaciers.

Acknowledgements:

This work was supported by Department of Science and Technology, Government of India, Climate Change Program (SPLICE) Grant DST/CCP/Aerosol/86/2017(C) and Science & Engineering Research Board (SERB) Grant (EMR/2015/000439) to I.S. Sen. S.N. is thankful for the IIT-Kanpur PhD scholarship. We thank Indian Institute of Technology-Kanpur (IIT-Kanpur), National Ocean Sciences Accelerator Mass Spectrometer (NOSAMS), Woods Hole Oceanographic Institution (WHOI), and Durham University for providing access to instrumentation and support. DS acknowledges the Total Endowment Fund and the Dida Scholarship of CUG, Wuhan. MFA acknowledges INSPIRE Faculty grant from DST-INPSIRE, Government of India. We thank 4 anonymous reviewers for their constructive comments that helped improve this contribution.

Contributions

I.S.S. conceived the study. S.N. and M.F.A did the field work. S.N. performed laboratory measurements. S.N., I.S.S., V.V. and S.K.P. developed the air mass back trajectory models. S.N., I.S.S., V.G., V.V., A.K.A., A.K.S. and D.S. analysed the data. R.A.C. and M.B. contributed to radiogenic isotope analysis and discussions. S.N. and I.S.S. wrote the paper with input from all authors.

Supplementary Materials:

Figures S1-S5 and Table S1

References

(1) Zemp, M.; Huss, M.; Thibert, E.; Eckert, N.; McNabb, R.; Huber, J.; Barandun, M.; Machguth, H.; Nussbaumer, S. U.; Gärtner-Roer, I.; Thomson, L.; Paul, F.; Maussion, F.; Kutuzov, S.; Cogley, J. G. Global Glacier Mass Changes and Their Contributions to Sea-Level Rise from 1961 to 2016. *Nature***2019**, *568* (7752), 382–386.

341 https://doi.org/10.1038/s41586-019-1071-0.
342 (2) Maurer, J. M.; Schaefer, J. M.; Rupper, S.; Corley, A. Acceleration of Ice Loss across the
343 Himalayas over the Past 40 Years. *Sci. Adv.***2019**, *5* (6), 1–12.
344 https://doi.org/10.1126/sciadv.aav7266.
345 (3) Lau, W. K. M.; Kim, M.K..; Kim, K.M.; Lee, W.S. Enhanced Surface Warming and
346 Accelerated Snow Melt in the Himalayas and Tibetan Plateau Induced by Absorbing
347 Aerosols. *Environ. Res. Lett.***2010**, *5* (2), 025204. https://doi.org/10.1088/1748-
348 9326/5/2/025204.
349 (4) Prasad, A. K.; S. Yang, K. H.; El-Askary, H. M.; Kafatos, M. Melting of Major Glaciers
350 in the Western Himalayas: Evidence of Climatic Changes from Long Term MSU Derived
351 Tropospheric Temperature Trend (1979-2008). *Ann. Geophys.***2009**, *27* (12), 4505–4519.
352 https://doi.org/10.5194/angeo-27-4505-2009.
353 (5) Santra, S.; Verma, S.; Fujita, K.; Chakraborty, I.; Boucher, O.; Takemura, T.; Burkhart, J.
354 F.; Matt, F.; Sharma, M. Simulations of Black Carbon (BC) Aerosol Impact over Hindu Kush
355 Himalayan Sites: Validation, Sources, and Implications on Glacier Runoff. *Atmos. Chem.*
356 *Phys.***2019**, *19* (4), 2441–2460. https://doi.org/10.5194/acp-19-2441-2019.
357 (6) Ming, J.; Wang, Y.; Du, Z.; Zhang, T.; Guo, W.; Xiao, C.; Xu, X.; Ding, M.; Zhang, D.;
358 Yang, W. Widespread Albedo Decreasing and Induced Melting of Himalayan Snow and Ice in
359 the Early 21st Century. *PLoS One***2015**, *10* (6), 1–13.
360 https://doi.org/10.1371/journal.pone.0126235.
361 (7) Xu, Y.; Ramanathan, V.; Washington, W. M. Observed High-Altitude Warming and
362 Snow Cover Retreat over Tibet and the Himalayas Enhanced by Black Carbon Aerosols.
363 *Atmos. Chem. Phys. Discuss.***2015**, *15* (13), 19079–19109. https://doi.org/10.5194/acpd-15-
364 19079-2015.
365 (8) Skiles, S. M. K.; Painter, T. Daily Evolution in Dust and Black Carbon Content, Snow
366 Grain Size, and Snow Albedo during Snowmelt, Rocky Mountains, Colorado. *J.*
367 *Glaciol.***2017**, *63* (237), 118–132. https://doi.org/10.1017/jog.2016.125.
368 (9) He, C.; Liou, K. N.; Takano, Y.; Chen, F.; Barlage, M. Enhanced Snow Absorption and
369 Albedo Reduction by Dust-Snow Internal Mixing: Modeling and Parameterization. *J. Adv.*
370 *Model. Earth Syst.***2019**, *11* (11), 3755–3776. https://doi.org/10.1029/2019MS001737.
371 (10) Kuchiki, K.; Aoki, T.; Niwano, M.; Matoba, S.; Kodama, Y.; Adachi, K. Elemental

372 Carbon, Organic Carbon, and Dust Concentrations in Snow Measured with Thermal Optical
373 and Gravimetric Methods: Variations during the 2007–2013 Winters at Sapporo, Japan.*J.*
374 *Geophys. Res. Atmos.***2015**, *120*, 868–882. https://doi.org/doi:10.1002/2014JD022144.
375 (11) Zhang, Y.; Kang, S.; Gao, T.; Schmale, J.; Liu, Y.; Zhang, W.; Guo, J.; Du, W.; Hu, Z.;
376 Cui, X.; Sillanpää, M. Dissolved Organic Carbon in Snow Cover of the Chinese Altai
377 Mountains, Central Asia: Concentrations, Sources and Light-Absorption Properties. *Sci. Total*
378 *Environ.***2019**, *647*, 1385–1397. https://doi.org/10.1016/j.scitotenv.2018.07.417.
379 (12) Yasunari, T. J.; Koster, R. D.; Lau, W. K. M.; Kim, K. Impact of Snow Darkening via
380 Dust, Black Carbon, and Organic Carbon on Boreal Spring Climate in the Earth System. *J.*
381 *Geophys. Res. Atmos. Res.***2015**, *120*, 5485–5503. https://doi.org/10.1002/ 2014JD022977.
382 (13) He, C.; Flanner, M. G.; Chen, F.; Barlage, M.; Liou, K. N.; Kang, S.; Ming, J.; Qian, Y.
383 Black Carbon-Induced Snow Albedo Reduction over the Tibetan Plateau: Uncertainties from
384 Snow Grain Shape and Aerosol-Snow Mixing State Based on an Updated SNICAR Model.
385 *Atmos. Chem. Phys.***2018**, *18* (15), 11507–11527. https://doi.org/10.5194/acp-18-11507-2018.
386 (14) Ming, J.; Cachier, H.; Xiao, C.; Qin, D.; Kang, S.; Hou, S.; Xu, J. Black Carbon Record
387 Based on a Shallow Himalayan Ice Core and Its Climatic Implications. *Atmos. Chem.*
388 *Phys.***2008**, *8* (5), 1343–1352. https://doi.org/10.5194/acp-8-1343-2008.
389 (15) Schmale, J.; Flanner, M.; Kang, S.; Sprenger, M.; Zhang, Q.; Guo, J.; Li, Y.;
390 Schwikowski, M.; Farinotti, D. Modulation of Snow Reflectance and Snowmelt from Central
391 Asian Glaciers by Anthropogenic Black Carbon. *Sci. Rep.***2017**, *7*, 1–10.
392 https://doi.org/10.1038/srep40501.
393 (16) Kaspari, S.; Painter, T. H.; Gysel, M.; Skiles, S. M.; Schwikowski, M. Seasonal and
394 Elevational Variations of Black Carbon and Dust in Snow and Ice in the Solu-Khumbu, Nepal
395 and Estimated Radiative Forcings. *Atmos. Chem. Phys.***2014**, *14* (15), 8089–8103.
396 https://doi.org/10.5194/acp-14-8089-2014.
397 (17) Yan, F.; He, C.; Kang, S.; Chen, P.; Hu, Z.; Han, X.; Gautam, S.; Yan, C.; Zheng, M.;
398 Sillanpää, M.; Raymond, P. A.; Li, C. Deposition of Organic and Black Carbon: Direct
399 Measurements at Three Remote Stations in the Himalayas and Tibetan Plateau. *J. Geophys.*
400 *Res. Atmos.***2019**, *124* (16), 9702–9715. https://doi.org/10.1029/2019JD031018.
401 (18) Xu, B.; Yao, T.; Liu, X.; Wang, N. Elemental and Organic Carbon Measurements with a
402 Two-Step Heating-Gas Chromatography System in Snow Samples from the Tibetan Plateau.

403 *Ann. Glaciol.***2006**, *43*, 257–262. https://doi.org/10.3189/172756406781812122.
404 (19) Chen, M.; Zeng, C.; Zhang, F.; Kang, S.; Li, C. Characteristics of Dissolved Organic
405 Matter from a Transboundary Himalayan Watershed: Relationships with Land Use, Elevation,
406 and Hydrology. *ACS Earth Sp. Chem.***2020**, *4* (3), 449–456.
407 https://doi.org/10.1021/acsearthspacechem.9b00329.
408 (20) Ohara, T.; Akimoto, H.; Kurokawa, J.; Horii, N.; Yamaji, K.; Yan, X.; Ohara, T.; Akimoto,
409 H.; Kurokawa, J.; Horii, N.; Yamaji, K.; Asian, A. An Asian Emission Inventory of
410 Anthropogenic Emission Sources for the Period 1980 – 2020. *Atmos. Chem. Phys.*
411 *Discuss.***2007**, *7* (3), 6843–6902.
412 (21) Ji, Z.; Kang, S.; Cong, Z.; Zhang, Q.; Yao, T. Simulation of Carbonaceous Aerosols over
413 the Third Pole and Adjacent Regions: Distribution, Transportation, Deposition, and Climatic
414 Effects. *Clim. Dyn.***2015**, *45* (9–10), 2831–2846. https://doi.org/10.1007/s00382-015-2509-1.
415 (22) Hamilton, T. L.; Havig, J. Primary Productivity of Snow Algae Communities on
416 Stratovolcanoes of the Pacific Northwest. *Geobiology***2017**, *15* (2), 280–295.
417 https://doi.org/10.1111/gbi.12219.
418 (23) Stibal, M.; Box, J. E.; Cameron, K. A.; Langen, P. L.; Yallop M. L;, Mottram, R. H.;
419 Khan, A. L., Molotch, N. P.; Chrismas, N. A. M.; Quaglia, F. C.; Remias, D.; Smeets, C. J.
420 P. P.; Broeke, M. R. van den.; Ryan, J. C.; Hubbard, A.; Tranter, M.; As, D. van.; Ahlstrøm,
421 A. P. Algae Drive Enhanced Darkening of Bare Ice on the Greenland Ice Sheet. *Geophys. Res.*
422 *Lett.***2017**, *44* (11), 463–471. https://doi.org/10.1002/2017GL075958.
423 (24) Giesen, R. H.; Oerlemans, J. Climate-Model Induced Differences in the 21st Century
424 Global and Regional Glacier Contributions to Sea-Level Rise. *Clim. Dyn.***2013**, *41* (11–12),
425 3283–3300. https://doi.org/10.1007/s00382-013-1743-7.
426 (25) Li, C.; Bosch, C.; Kang, S.; Andersson, A.; Chen, P.; Zhang, Q.; Cong, Z.; Chen, B.; Qin,
427 D.; Gustafsson, Ö. Sources of Black Carbon to the Himalayan-Tibetan Plateau Glaciers. *Nat.*
428 *Commun.***2016**, *7*, 1–7. https://doi.org/10.1038/ncomms12574.
429 (26) Soni, A.; Decesari, S.; Shridhar, V.; Prabhu, V.; Panwar, P.; Marinoni, A. Investigation
430 of Potential Source Regions of Atmospheric Black Carbon in the Data Deficit Region of the
431 Western Himalayas and Its Foothills. *Atmos. Pollut. Res.***2019**, *10* (6), 1832–1842.
432 https://doi.org/10.1016/j.apr.2019.07.015.
433 (27) Alvarado, M. J.; Winijkul, E.; Adams-Selin, R.; Hunt, E.; Brodowski, C.; Lonsdale, C.

R.; Shindell, D. T.; Faluvegi, G.; Kleiman, G.; Mosier, T. M.; Kumar, R. Sources of Black Carbon Deposition to the Himalayan Glaciers in Current and Future Climates. *J. Geophys. Res. Atmos.***2018**, *123* (14), 7482–7505. https://doi.org/https://doi.org/10.1029/2018JD029049.

(28) Kopacz, M.; Mauzerall, D. L.; Wang, J.; Leibensperger, E. M.; Henze, D. K.; Singh, K. Origin and Radiative Forcing of Black Carbon Transported to the Himalayas and Tibetan Plateau. *Atmos. Chem. Phys.***2011**, *11* (6), 2837–2852. https://doi.org/10.5194/acp-11-2837-2011.

(29) Kapnick, S. B.; Delworth, T. L.; Ashfaq, M.; Malyshev, S.; Milly, P. C. D. Snowfall Less Sensitive to Warming in Karakoram than in Himalayas Due to a Unique Seasonal Cycle. *Nat. Geosci.***2014**, *7* (11), 834–840. https://doi.org/10.1038/ngeo2269.

(30) Lutz, A. F.; Immerzeel, W. W.; Shrestha, A. B.; Bierkens, M. F. P. Consistent Increase in High Asia's Runoff Due to Increasing Glacier Melt and Precipitation. *Nat. Clim. Chang.***2014**, *4* (7), 587–592. https://doi.org/10.1038/nclimate2237.

(31) Maussion, F.; Scherer, D.; Mölg, T.; Collier, E.; Curio, J.; Finkelnburg, R. Precipitation Seasonality and Variability over the Tibetan Plateau as Resolved by the High Asia Reanalysis. *J. Clim.***2014**, *27* (5), 1910–1927. https://doi.org/10.1175/JCLI-D-13-00282.1.

(32) Frey, H.; Machguth, H.; Huss, M.; Huggel, C.; Bajracharya, S.; Bolch, T.; Kulkarni, A.; Linsbauer, A.; Salzmann, N.; Stoffel, M. Estimating the Volume of Glaciers in the Himalayan-Karakoram Region Using Different Methods. *Cryosphere***2014**, *8* (6), 2313–2333. https://doi.org/10.5194/tc-8-2313-2014.

(33) Nizam, S.; Sen, I. S. Effect of Southwest Monsoon Withdrawal on Mass Loading and Chemical Characteristics of Aerosols in an Urban City over the Indo-Gangetic Basin. *ACS Earth Sp. Chem.***2018**, *2* (4), 347–355. https://doi.org/10.1021/acsearthspacechem.7b00140.

(34) Rosenheim, B. E.; Day, M. B.; Domack, E.; Schrum, H.; Benthien, A.; Hayes, J. M. Antarctic Sediment Chronology by Programmed-Temperature Pyrolysis: Methodology and Data Treatment. *Geochemistry, Geophys. Geosystems***2008**, *9* (4), 1–16. https://doi.org/10.1029/2007GC001816.

(35) Hemingway, J. D.; Rothman, D. H.; Rosengard, S. Z.; Galy, V. V. Technical Note: An Inverse Method to Relate Organic Carbon Reactivity to Isotope Composition from Serial Oxidation. *Biogeosciences***2017**, *14* (22), 5099–5114. https://doi.org/10.5194/bg-14-5099-2017.

(36) Hemingway, J. D.; Galy, V. V.; Gagnon, A. R.; Grant, K. E.; Rosengard, S. Z.; Soulet, G.; Zigah, P. K.; McNichol, A. P. Assessing the Blank Carbon Contribution, Isotope Mass Balance, and Kinetic Isotope Fractionation of the Ramped Pyrolysis/Oxidation Instrument at Nosams. *Radiocarbon***2017**, *59* (1), 179–193. https://doi.org/10.1017/RDC.2017.3.

(37) J. D. Hemingway (2016). Rampedpyrox: Open-Source Tools for Thermoanalytical Data Analysis. Http://Pypi.Python.Org/Pypi/Rampedpyrox (Online Accessed 2019-06-25).

(38) Belshaw, N. .; Freedman, P. .; O'Nions, R. .; Frank, M.; Guo, Y. A New Variable Dispersion Double-Focusing Plasma Mass Spectrometer with Performance Illustrated for Pb Isotopes. *Int. J. Mass Spectrom.***1998**, *181* (1–3), 51–58. https://doi.org/10.1016/S1387-3806(98)14150-7.

(39) Todt, W.; Cliff, R. A.; Hanser, A.; Hofmann, A. W. Evaluation of a 202 Pb- 205 Pb Double Spike for High - Precision Lead Isotope Analysis. In *Earth Processes: Reading the Isotopic Code*; A. Basu, S. H., Ed.; Blackwell Publishing Limited: AGU, Washington, D.C., 1995; Vol. 95, pp 429–437. https://doi.org/10.1029/GM095p0429.

(40) Hemingway, J. D.; Hilton, R. G.; Hovius, N.; Eglinton, T. I.; Haghipour, N.; Wacker, L.; Chen, M. C.; Galy, V. V. Microbial Oxidation of Lithospheric Organic Carbon in Rapidly Eroding Tropical Mountain Soils. *Science (80).***2018**, *360* (6385), 209–212. https://doi.org/10.1126/science.aao6463.

(41) Pendergraft, M. A.; Rosenheim, B. E. Varying Relative Degradation Rates of Oil in Different Forms and Environments Revealed by Ramped Pyrolysis. *Environ. Sci. Technol.***2014**, *48* (18), 10966–10974. https://doi.org/10.1021/es501354c.

(42) Galy, V.; Eglinton, T. Protracted Storage of Biospheric Carbon in the Ganges-Brahmaputra Basin. *Nat. Geosci.***2011**, *4* (12), 843–847. https://doi.org/10.1038/ngeo1293.

(43) Katherine L. French, Christopher J. Hein, Negar Haghipour, Lukas Wacker, Hermann R. Kudrass, Timothy I. Eglinton, V. G. Millennial Soil Retention of Terrestrial Organic Matter Deposited in the BengalFan. *Sci. Rep.***2018**, *8*, 11997. https://doi.org/10.1038/s41598-018-30091-8.

(44) Galy, V.; France-Lanord, C.; Beyssac, O.; Faure, P.; Kudrass, H.; Palhol, F. Efficient Organic Carbon Burial in the Bengal Fan Sustained by the Himalayan Erosional System. *Nature***2007**, *450* (7168), 407–410. https://doi.org/10.1038/nature06273.

(45) McCrimmon, D. O.; Bizimis, M.; Holland, A.; Ziolkowski, L. A. Supraglacial Microbes

Use Young Carbon and Not Aged Cryoconite Carbon. *Org. Geochem.***2018**, *118*, 63–72. https://doi.org/10.1016/j.orggeochem.2017.12.002.

(46) Musilova, M.; Tranter, M.; Bennett, S. A.; Wadham, J.; Anesio, A. M. Stable Microbial Community Composition on the Greenland Ice Sheet. *Front. Microbiol.***2015**, *6*, 1–10. https://doi.org/10.3389/fmicb.2015.00193.

(47) Agnihotri, R.; Mandal, T. K.; Karapurkar, S. G.; Naja, M.; Gadi, R.; Ahammmed, Y. N.; Kumar, A.; Saud, T.; Saxena, M. Stable Carbon and Nitrogen Isotopic Composition of Bulk Aerosols over India and Northern Indian Ocean. *Atmos. Environ.***2011**, *45* (17), 2828–2835. https://doi.org/10.1016/j.atmosenv.2011.03.003.

(48) Turekian, V. C.; MacKo, S.; Ballentine, D.; Swap, R. J.; Garstang, M. Causes of Bulk Carbon and Nitrogen Isotopic Fractionations in the Products of Vegetation Burns: Laboratory Studies. *Chem. Geol.***1998**, *152* (1–2), 181–192. https://doi.org/10.1016/S0009-2541(98)00105-3.

(49) Chen, X.; Kang, S.; Cong, Z.; Yang, J.; Ma, Y. Concentration, Temporal Variation, and Sources of Black Carbon in the Mt. Everest Region Retrieved by Real-Time Observation and Simulation. *Atmos. Chem. Phys.***2018**, *18* (17), 12859–12875. https://doi.org/10.5194/acp-18-12859-2018.

(50) Lee, K.; Hur, S. Do; Hou, S.; Burn-Nunes, L. J.; Hong, S.; Barbante, C.; Boutron, C. F.; Rosman, K. J. R. Isotopic Signatures for Natural versus Anthropogenic Pb in High-Altitude Mt. Everest Ice Cores during the Past 800years. *Sci. Total Environ.***2011**, *412–413*, 194–202. https://doi.org/10.1016/j.scitotenv.2011.10.002.

(51) Brun, F.; Berthier, E.; Wagnon, P.; Kääb, A.; Treichler, D. A Spatially Resolved Estimate of High Mountain Asia Glacier Mass Balances from 2000 to 2016. *Nat. Geosci.***2017**, *10* (9), 668–673. https://doi.org/10.1038/ngeo2999.

(52) Azam, M. F.; Ramanathan, A. L.; Wagnon, P.; Vincent, C.; Linda, A.; Berthier, E.; Sharma, P.; Mandal, A.; Angchuk, T.; Singh, V. B.; Pottakkal, J. G. Meteorological Conditions, Seasonal and Annual Mass Balances of Chhota Shigri Glacier, Western Himalaya, India. *Ann. Glaciol.***2016**, *57* (71), 328–338. https://doi.org/10.3189/2016AoG71A570.

(53) Kumar, A.; Attri, A. K. Biomass Combustion a Dominant Source of Carbonaceous Aerosols in the Ambient Environment of Western Himalayas. *Aerosol Air Qual. Res.***2016**, *16*

(3), 519–529. https://doi.org/10.4209/aaqr.2015.05.0284.

(54) Saxena, M.; Sharma, S. K.; Tomar, N.; Ghayas, H.; Sen, A.; Garhwal, R. S.; Gupta, N. C.; Mandal, T. K. Residential Biomass Burning Emissions over Northwestern Himalayan Region of India: Chemical Characterization and Budget Estimation. *Aerosol Air Qual. Res.***2016**, *16* (3), 504–518. https://doi.org/10.4209/aaqr.2015.04.0237.

(55) Li, C.; Kang, S.; Yan, F. Importance of Local Black Carbon Emissions to the Fate of Glaciers of the Third Pole. *Environ. Sci. Technol.***2018**, *52* (24), 14027–14028. https://doi.org/10.1021/acs.est.8b06285.

(56) Streets, D. G.; Bond, T. C.; Lee, T.; Jang, C. On the Future of Carbonaceous Aerosol Emissions. *J. Geophys. Res. D Atmos.***2004**, *109* (24), 1–19. https://doi.org/10.1029/2004JD004902.

(57) Lamb, A. L.; Wilson, G. P.; Leng, M. J. A Review of Coastal Palaeoclimate and Relative Sea-Level Reconstructions Using Δ13C and C/N Ratios in Organic Material. *Earth-Science Rev.***2006**, *75* (1–4), 29–57. https://doi.org/10.1016/j.earscirev.2005.10.003.

(58) Havig, J. R.; Hamilton, T. L. Snow Algae Drive Productivity and Weathering at Volcanic Rock-Hosted Glaciers. *Geochim. Cosmochim. Acta***2019**, *247*, 220–242. https://doi.org/10.1016/j.gca.2018.12.024.

(59) Leu, E.; Wiktor, J.; Søreide, J. E.; Berge, J.; Falk-Petersen, S. Increased Irradiance Reduces Food Quality of Sea Ice Algae. *Mar. Ecol. Prog. Ser.***2010**, *411*, 49–60. https://doi.org/10.3354/meps08647.

(60) Rabha, S.; Saikia, J.; Subramanyam, K. S. V.; Hower, J. C.; Hood, M. M.; Khare, P.; Saikia, B. K. Geochemistry and Nanomineralogy of Feed Coals and Their Coal Combustion Residues from Two Different Coal-Based Industries in Northeast India. *Energy and Fuels***2018**, *32* (3), 3697–3708. https://doi.org/10.1021/acs.energyfuels.7b03907.

(61) Yang, W. High Precision Determination of Trace Elements in Crude Oils by Using Inductively Coupled Plasma Optical Emission Spectrometry and Inductively Coupled Plasma-Mass Spectrometry, University of Houston, 2014. https://doi.org/http://hdl.handle.net/10657/1615.

(62) Clift, P. D.; Lee J.I; Hildebrand, P.; Shimizu, N.; Layne, G. D.; Blusztajn, J.; Blum, J. D.; Garzanti, E.; Ali, A. Nd and Pb Isotope Variability in the Indus River System : Implications for

Sediment Provenance and Crustal Heterogeneity in the Western Himalaya. *Earth Planet. Sci. Lett.***2002**, *200*, 91–106. https://doi.org/https://doi.org/10.1016/S0012-821X(02)00620-9.

(63) Ghosh, N.; Basu, A. R.; Bhargava, O. N.; Shukla, U. K.; Ghatak, A.; Garzione, C. N.; Ahluwalia, A. D. Catastrophic Environmental Transition at the Permian-Triassic Neo-Tethyan Margin of Gondwanaland: Geochemical, Isotopic and Sedimentological Evidence in the Spiti Valley, India. *Gondwana Res.***2016**, *34*, 324–345. https://doi.org/10.1016/j.gr.2015.04.006.

(64) Deb, M.; Thorpe, R. I.; Cumming, G. L.; Wagner, P. A. Age, Source and Stratigraphic Implications of Pb Isotope Data for Conformable, Sediment-Hosted, Base Metal Deposits in the Proterozoic Aravalli-Delhi Orogenic Belt, Northwestern India. *Precambrian Res.***1989**, *43* (1–2), 1–22. https://doi.org/10.1016/0301-9268(89)90002-8.

(65) Gelly, R.; Fekiacova, Z.; Guihou, A.; Doelsch, E.; Deschamps, P.; Keller, C. Lead, Zinc, and Copper Redistributions in Soils along a Deposition Gradient from Emissions of a Pb-Ag Smelter Decommissioned 100 years Ago. *Sci. Total Environ.***2019**, *665*, 502–512. https://doi.org/10.1016/j.scitotenv.2019.02.092.

(66) Gariépy, C.; Allègre, C. J.; Rong Hua Xu. The Pb-Isotope Geochemistry of Granitoids from the Himalaya-Tibet Collision Zone: Implications for Crustal Evolution. *Earth Planet. Sci. Lett.***1985**, *74* (2–3), 220–234. https://doi.org/10.1016/0012-821X(85)90023-8.

(67) Das, R.; Bin Mohamed Mohtar, A. T.; Rakshit, D.; Shome, D.; Wang, X. Sources of Atmospheric Lead (Pb) in and around an Indian Megacity. *Atmos. Environ.***2018**, *193*, 57–65. https://doi.org/10.1016/j.atmosenv.2018.08.062.

(68) Wang, Z.; Dwyer, G. S.; Coleman, D. S.; Vengosh, A. Lead Isotopes as a New Tracer for Detecting Coal Fly Ash in the Environment. *Environ. Sci. Technol. Lett.***2019**, 6 (12), 714-719. https://doi.org/10.1021/acs.estlett.9b00512.

(69) Kumar, S.; Aggarwal, S. G.; Sarangi, B.; Malherbe, J.; Barre, J. P. G.; Berail, S.; Séby, F.; Donard, O. F. X. Understanding the Influence of Open-Waste Burning on Urban Aerosols Using Metal Tracers and Lead Isotopic Composition. *Aerosol Air Qual. Res.***2018**, *18* (9), 2433–2446. https://doi.org/10.4209/aaqr.2017.11.0510.

(70) Kumar, S.; Aggarwal, S. G.; Malherbe, J.; Barre, J. P. G.; Berail, S.; Gupta, P. K.; Donard, O. F. X. Tracing Dust Transport from Middle-East over Delhi in March 2012 Using Metal and Lead Isotope Composition. *Atmos. Environ.***2016**, *132*, 179–187. https://doi.org/10.1016/j.atmosenv.2016.03.002.

(71) Sen, I. S.; Bizimis, M.; Tripathi, S. N.; Paul, D. Lead Isotopic Fingerprinting of Aerosols to Characterize the Sources of Atmospheric Lead in an Industrial City of India. *Atmos. Environ.***2016**, *129*, 27–33. https://doi.org/10.1016/j.atmosenv.2016.01.005.

(72) A. Bollhoffer and K. J. R. Rosman. The Temporal Stability in Lead Isotopic Signatures at Selected Sites in the Southern and Northern Hemispheres. *Geochim. Cosmochim. Acta***2002**, *66* (8), 1375–1386. https://doi.org/https://doi.org/10.1016/S0016-7037(01)00862-6.

(73) Abouchami, W.; Näthe, K.; Kumar, A.; Galer, S. J. G.; Jochum, K. P.; Williams, E.; Horbe, A. M. C.; Rosa, J. W. C.; Balsam, W.; Adams, D.; Mezger, K.; Andreae, M. O. Geochemical and Isotopic Characterization of the Bodélé Depression Dust Source and Implications for Transatlantic Dust Transport to the Amazon Basin. *Earth Planet. Sci. Lett.***2013**, *380*, 112–123. https://doi.org/10.1016/J.EPSL.2013.08.028.

(74) S. S. Sun. Lead Isotopic Studty of Young Volcanic Rocks from Mid-Ocean Ridges, Ocean Islands and Islands Arcs. *Phil. Trans. R. Soc. A.***1980**, *297*, 409–445. https://doi.org/https://doi.org/10.1098/rsta.1980.0224.

(75) Rousseau, D. D.; Chauvel, C.; Sima, A.; Hatté, C.; Lagroix, F.; Antoine, P.; Balkanski, Y.; Fuchs, M.; Mellett, C.; Kageyama, M.; Ramstein, G.; Lang, A. European Glacial Dust Deposits: Geochemical Constraints on Atmospheric Dust Cycle Modeling. *Geophys. Res. Lett.***2014**, *41* (21), 7666–7674. https://doi.org/10.1002/2014GL061382.

(76) Ferrat, M.; Weiss, D. J.; Dong, S.; Large, D. J.; Spiro, B.; Sun, Y.; Gallagher, K. Lead Atmospheric Deposition Rates and Isotopic Trends in Asian Dust during the Last 9.5kyr Recorded in an Ombrotrophic Peat Bog on the Eastern Qinghai-Tibetan Plateau. *Geochim. Cosmochim. Acta***2012**, *82*, 4–22. https://doi.org/10.1016/j.gca.2010.10.031.

(77) Bory, A. J. M.; Abouchami, W.; Galer, S. J. G.; Svensson, A.; Christensen, J. N.; Biscaye, P. E. A Chinese Imprint in Insoluble Pollutants Recently Deposited in Central Greenland as Indicated by Lead Isotopes. *Environ. Sci. Technol.***2014**, *48* (3), 1451–1457. https://doi.org/10.1021/es4035655.

(78) Biscaye, P. E.; Grousset, F. E.; Revel, M.; Gaast, S. V. D.; Zielinski, G. A.; Vaars, A.; Kukla, G. Asian Provenance of Glacial Dust (Stage 2) in the GISP2 Ice Core, Summit, Greenland. *J. Geophys. Res.***1997**, *102* (C12), 26315–26886. https://doi.org/https://doi.org/10.1029/97JC01249.

(79) Kurkjian, R.; Dunlap, C.; Flegal, A. R. Lead Isotope Tracking of Atmospheric Response

619 to Post-Industrial Conditions in Yerevan, Armenia. *Atmos. Environ.***2002**, *36* (8), 1421–1429.
620 https://doi.org/10.1016/S1352-2310(01)00499-X.
621 (80) Hansmann, W.; Koppel, V. Lead-Isotopes as Tracers of Pollutants in Soils. *Chem.*
622 *Geol.***2000**, *171*, 123–144. https://doi.org/https://doi.org/10.1016/S0009-2541(00)00230-8.
623 (81) Chow, T. J.; Johnstone, M. S. Lead Isotopes in Gasoline and Aerosols of Los Angeles
624 Basin, California. *Science (80).***1965**, *147* (3657), 502–503.
625 https://doi.org/10.1126/science.147.3657.502
626 (82) Monna, F.; Lancelot,J.; Croudace, I. W.; Cundy, A. B; Lewis J. Pb Isotopic Composition
627 of Airborne Particulate Material from France and the Southern United Kingdom:
628 Implications for Pb Pollution Sources in Urban Areas. *Environ. Sci. Technol.***1997**, *31* (8),
629 2277–2286.
630 (83) Sangster, D. F.; Outridge, P. M.; Davis, W. J. Stable Lead Isotope Characteristics of Lead
631 Ore Deposits of Environmental Significance. *Environ. Rev.***2002**, *8* (2), 115–147.
632 https://doi.org/10.1139/er-8-2-115.
633

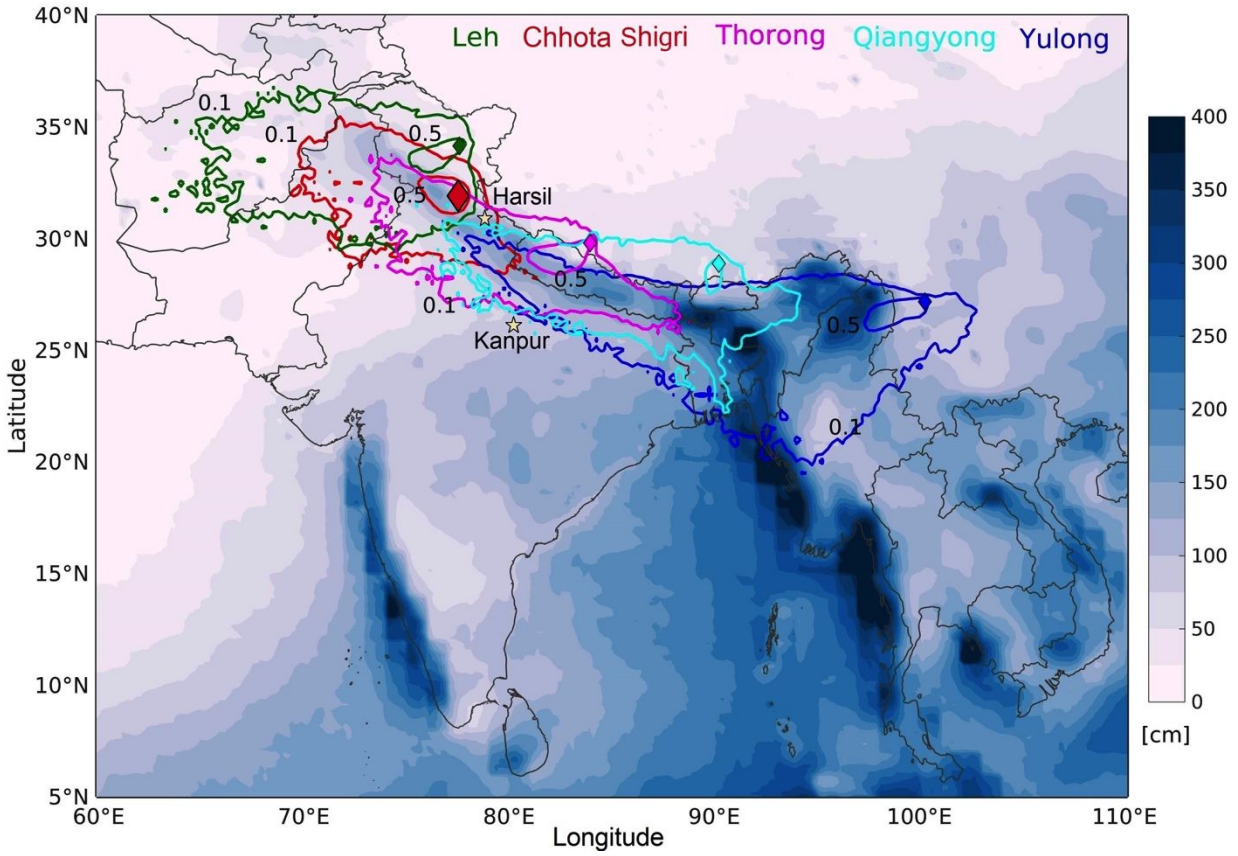

Figure 1. Climatological rainfall (TRMM_3B42_v7) with overlain trajectory density plot for few glaciers in the Himalayan-Tibetan Plateau region. The line contours represent the fractional number of trajectories passing through a particular grid of spatial-resolution (0.25^{o} x 0.25^{o}). For clarity, only two contours (of values 0.5 and 0.1) are shown for each receptor site. Here, 168-h HYSPLIT back trajectory starting from each of the five-receptor site for every hour (24x365) of the year 2016 were used. Thorong, Qiangyong, and Yulong sites have ~50%fossil fuel derived carbon.[25] Stars represent the aerosol sampling location and highlighted large polygon is our glacier-sampling site. The figure shows that there is a marked difference between the rainfall amounts between the western and eastern Himalayan glacier sites with eastern Himalaya obtaining higher rainfall. The 0.5 and 0.1 contour intervals show that the western Himalayan glacier sites are mostly influenced by air mass from western parts of the Himalaya, whereas central and eastern Himalayan glaciers are impacted by air mass from the Indo-Gangetic Plains (IGP) which is characterized by high level of anthropogenic activities (Figure S1).Seasonal trajectory density plots further show that wind trajectory origin is near similar irrespective of the seasons with most trajectories originating over a small region around the studied glacier (Figure S2).

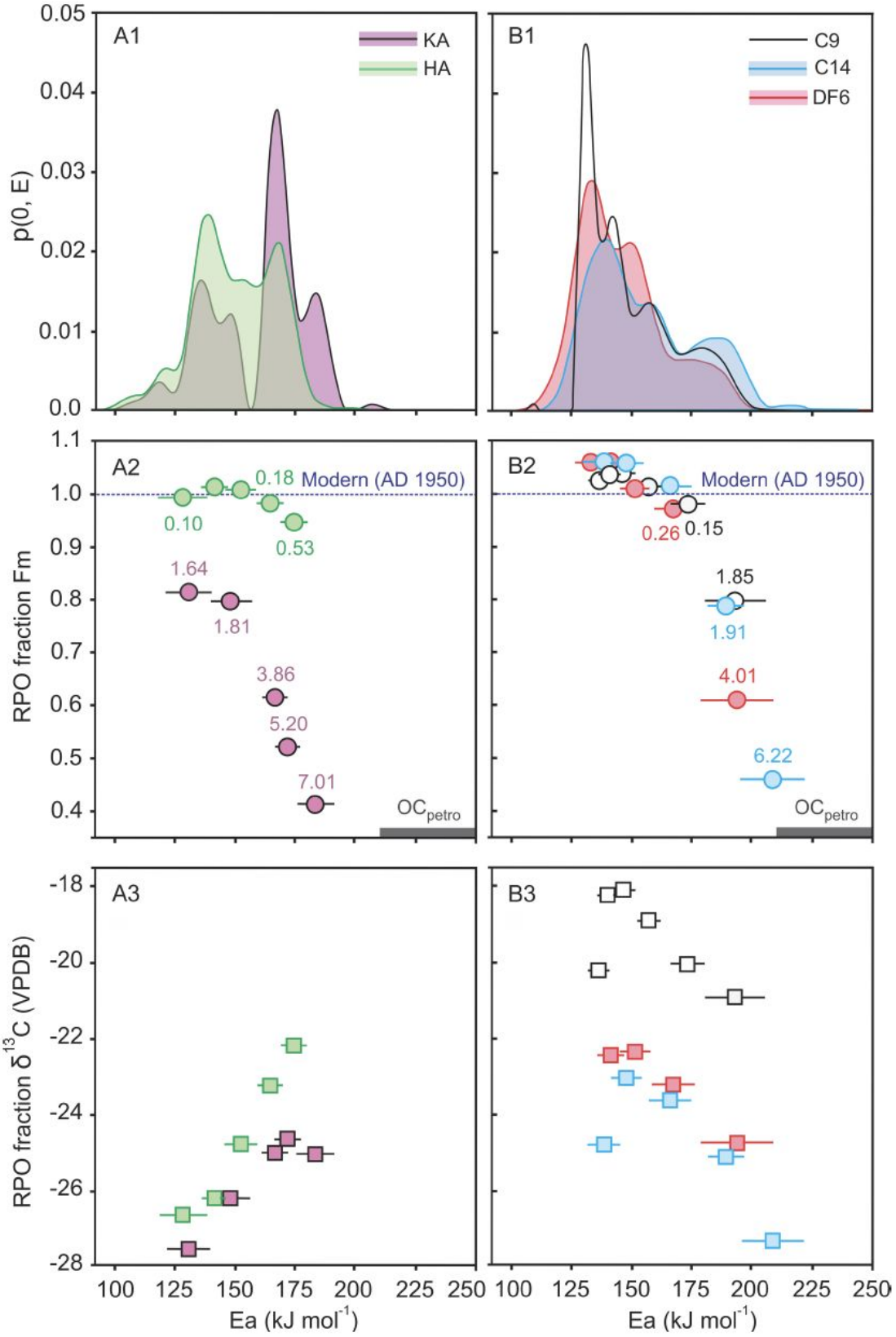
A1
KA
HA
B1
C9
C14
DF6
p(0, E)
A2
B2
Modern (AD 1950)
0.10
0.18
0.53
1.64
1.81
3.86
5.20
7.01
0.26
0.15
1.85
1.91
4.01
6.22
OC petro
RPO fraction Fm
A3
B3
RPO fraction δ13C (VPDB)
Ea (kJ mol-1)

652

653 **Figure 2. Apportionment of OC sources from RPO analysis**. OC activation energy (Ea)
654 distributions (p (0, E) of (A1) aerosol (Kanpur Aerosol: KA, Harsil Aerosol: HA) and (B1)
655 glacier samples (cryoconite: C9 and C14, moraine fine fraction: DF6). Radiocarbon (Fm in
656 fraction) composition of each RPO fraction of the samples with associated radiocarbon age (in
657 cal kyr BP) and stable carbon ($\delta^{13}C$ in ‰) are plotted in middle (A2 and B2) and lower panel
658 (A3 and B3) respectively. Peak reactivity at ca. 165 kJ mol-^{1} and associated low Fm value and
659 old ^{14}C ages highlights OC_{ff} contributions in KA. Low OC thermal recalcitrance (peak <150 kJ
660 mol^{-1}) and associated high Fm values and modern ages comparable to OC_{bio} and HA reflects
661 recently fixed sources. OC in glacier samples contain small contributions of high Ea material
662 reflecting binary mixing between a dilute petrogenic end member and a more concentrated
663 biomass/biospheric end member. Dashed line in both the middle panel represents modern
664 radiocarbon age.

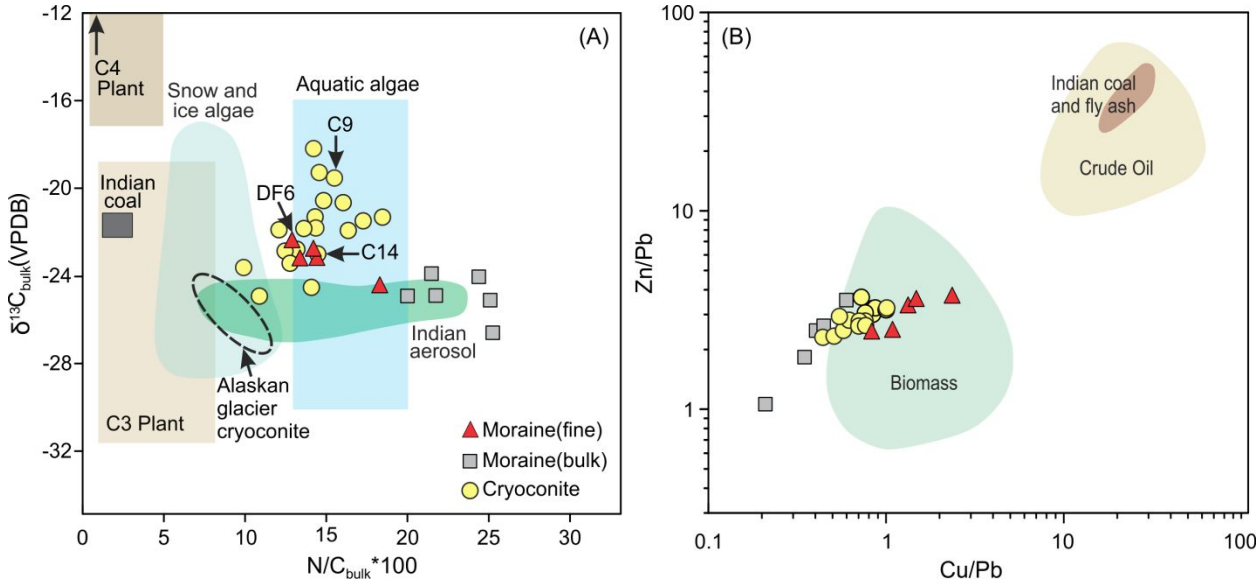

Figure 3.OC source inference from stable C isotopes, N/C and heavy metal ratios. (A) Bulk OC, elemental (N/C) and isotopic ($\delta^{13}C$) mixing diagram showing the composition of cryoconite and moraine samples compared to that of tentative endmembers. Nitrogen and ^{13}C enrichment in cryoconite compared to bulk moraine suggests mixing between ^{13}C-poor, N-poor OM characteristic of biomass and ^{13}C-rich, N-rich OM typical of algae/microbes dwelling on glacier surface. Linear mixing trend between fine and bulk moraine suggests mixing between petrogenic and biospheric input. Literature references: C3 plant, C4 plant and aquatic algae[57], snow and ice algae[22,58,59], Indian aerosol.[47] **(B)** Heavy metal ratios in glacier samples compared to biomass, Indian coal, flyash[60] and crude oil.[61]

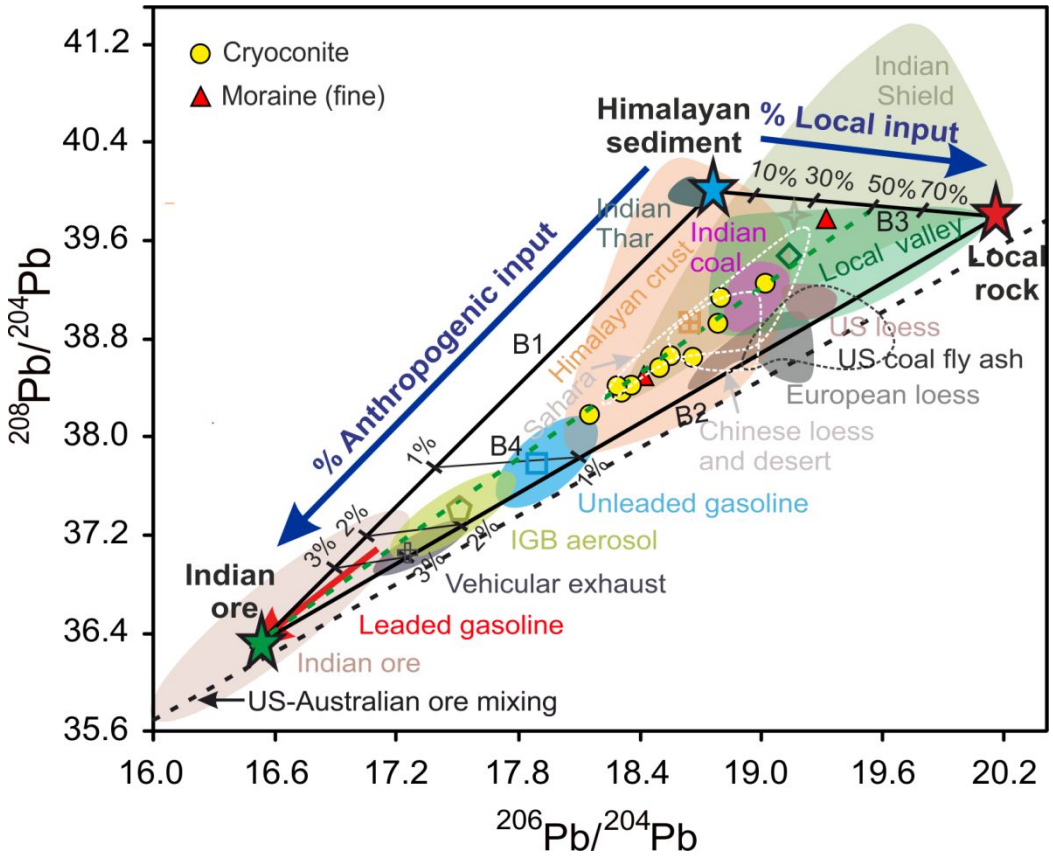

Figure 4. Mixing arrays in $^{206}Pb^{204}Pb$ versus $^{208}Pb^{204}$ isotopic space. The yellow circles and red triangles are new data points; literature data is shown with colored fields and open symbols within the field denotes their average composition. Thick black, dashed green and black lines are 2-component mixing lines. The color-filled stars are end-member composition used in mixing calculations. The curves B1 and B2 defines mixing of Indian ore with Himalayan sediment (HS) and local crust (LC), respectively, while B3 represents mixing between LC and HS composition. Curves B4 is a mixing line between Indian ore with a sediment mixture comprising of 50% HS and 50% LC. We selected HS ($^{206}Pb/^{204}Pb$ = 18.81, $^{208}Pb/^{204}Pb$ = 39.99, Pb = 26.7 ppm)[62] and LC ($^{206}Pb^{204}Pb$ = 20.15, $^{208}Pb^{204}Pb$ = 39.79, Pb = 33 ppm)[63] as a natural source end member. As an anthropogenic source end member representative, Indian ore ($^{206}Pb/^{204}Pb$ = 16.42, $^{208}Pb/^{204}Pb$ = 37.27, Pb = 4000 ppm)[64,65] was chosen with the view that Pb used in various anthropogenic activities are mined from these ore inherit its source signature. Literature references for other regional source end-members are: Indian shield[66], Indian coal[67], US coal fly ash[68], IGB aerosol[69–72],Sahara[73,74], European loess[75], Chinese loess and desert[76–78], Thar[76], US loess[78], unleaded gasoline[79], vehicular exhaust[80], leaded gasoline[81,82] and US-Australian ore.[83]

693 **Table 1.** RPO analysis results for cryoconite (C9 and C14), moraine (DF6) and aerosol samples
694 (KA: Kanpur Aerosol, HA: Harsil Aerosol).

Sample-RPO fraction	T(°C) min	T(°C) max	m_F µg C	Ea (1 σ) (kJ mol^{-1})	Fm (2 σ) (fraction modern)	$\delta^{13}C$ (‰)	^{14}C age (calyr BP)
C9-F1	150	300	100.3	138 ± 6	1.0191 ± 0.0020	-20.57	>Modern
C9-F2	300	326	106.6	140 ± 4	1.0408 ± 0.0021	-18.37	>Modern
C9-F3	326	361	112.1	146 ± 7	1.0399 ± 0.0020	-18.07	>Modern
C9-F4	361	412	102.5	157 ± 8	1.0126 ± 0.0026	-18.77	>Modern
C9-F5	412	480	90.3	171 ± 9	0.9822 ± 0.0019	-20.03	145±15
C9-F6	480	794	88.0	191 ± 13	0.7947 ± 0.0021	-21.00	1850±20
C14-F1	150	318	136.4	136 ± 7	1.0563 ± 0.0021	-24.93	>Modern
C14-F2	318	375	135.0	148 ± 6	1.0529 ± 0.0021	-22.99	>Modern
C14-F3	375	465	135.0	165 ± 9	1.0137 ± 0.0023	-23.58	>Modern
C14-F4	465	560	100.0	188 ± 8	0.788 ± 0.0018	-25.1	1910±20
C14-F5	560	850	36.8	208 ± 14	0.4609 ± 0.0039	-27.17	6220±70
DF6-F1	150	298	108.0	132 ± 8	1.0461 ± 0.0022	-10.76	>Modern
DF6-F2	298	336	100.1	142 ± 6	1.0485 ± 0.0025	-22.43	>Modern
DF6-F3	336	387	109.0	153 ± 8	1.0063 ± 0.0023	-22.28	>Modern
DF6-F4	387	483	100.6	168 ± 10	0.9688 ± 0.0020	-23.17	255±15
DF6-F5	483	784	57.6	193 ± 15	0.6068 ± 0.0020	-24.71	4010±30
KA-F1	125	306	104.1	130 ± 11	0.8155 ± 0.0019	-27.66	1640±20
KA-F2	306	377	100.3	147 ± 10	0.7982 ± 0.0018	-26.17	1810±20
KA-F3	377	425	103.1	166 ± 6	0.6182 ± 0.0018	-25.11	3860±25
KA-F4	425	462	102.0	171 ± 6	0.5237 ± 0.0022	-24.60	5200±35
KA-F5	462	655	101.4	183 ± 8	0.4179 ± 0.0017	-24.91	7010±30
HA-F1	125	293	53.6	127 ± 11	0.9884 ± 0.0030	-26.83	95±25
HA-F2	293	335	51.9	142 ± 6	1.0096 ± 0.0036	-26.23	>Modern
HA-F3	335	385	52.8	152 ± 7	1.0029 ± 0.0033	-24.78	>Modern
HA-F4	385	439	52.1	165 ± 6	0.9775 ± 0.0033	-23.23	180±25
HA-F5	439	605	34.0	175 ± 7	0.9364 ± 0.0039	-22.13	530±35

m_F: Mass of carbon (as CO_2) contained in RPO fraction F

696 **Table 2.** Radiogenic lead isotope composition of selected cryoconite (Cx) and moraine (DF) samples.

Sample id	$^{208}Pb/^{204}Pb$	2SE	$^{207}Pb/^{204}Pb$	2SE	$^{206}Pb/^{204}Pb$	2SE	$^{207}Pb/^{206}Pb$	2SE
C1	38.91787	0.00546	15.70946	0.00182	18.78705	0.00159	0.83616	0.00003
C3	39.13549	0.00684	15.73477	0.00250	18.80094	0.00244	0.83691	0.00004
C5	39.23825	0.00680	15.74825	0.00218	19.02939	0.00224	0.82757	0.00005
C9	38.67497	0.00868	15.67102	0.00286	18.65789	0.00250	0.83991	0.00005
C11	38.67167	0.00520	15.68224	0.00166	18.55690	0.00178	0.84508	0.00003
C13	38.58314	0.00728	15.68314	0.00250	18.50767	0.00242	0.84740	0.00004
C14	38.38955	0.00552	15.65890	0.00204	18.32318	0.00202	0.85456	0.00003
C17	38.40762	0.00426	15.66683	0.00146	18.35741	0.00139	0.85343	0.00003
C18	38.40409	0.00630	15.65812	0.00242	18.30283	0.00202	0.85551	0.00004
C19	38.21132	0.00476	15.63569	0.00164	18.15303	0.00163	0.86133	0.00003
DF6	38.42784	0.00562	15.68993	0.00208	18.40597	0.00196	0.85239	0.00005
DF12	39.74669	0.00720	15.76498	0.00246	19.32824	0.00226	0.81567	0.00003

Note: Total Pb concentration in blank = 0.2 ± 0.16 ppb (1 S.D., n=4), Reproducibility uncertainty level = 1σ

698 **TOC ART**

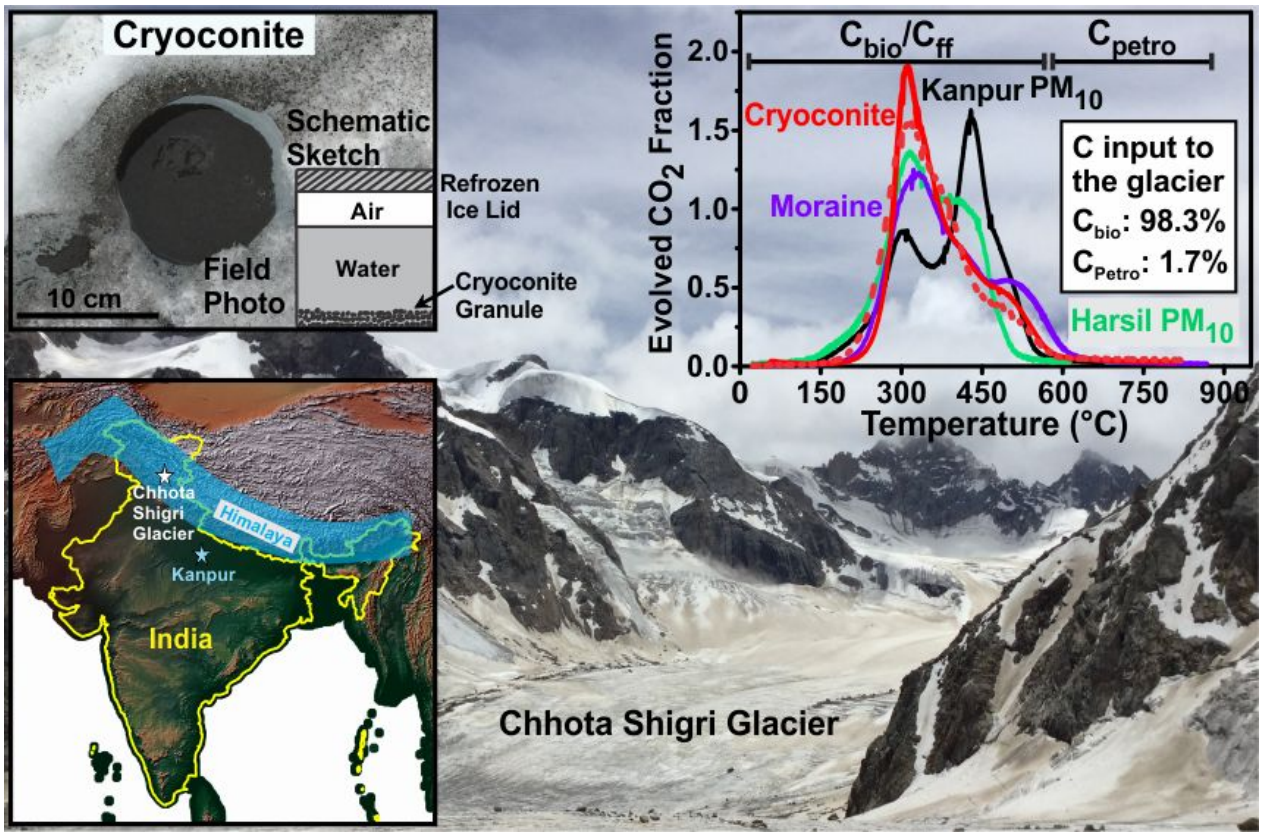

699

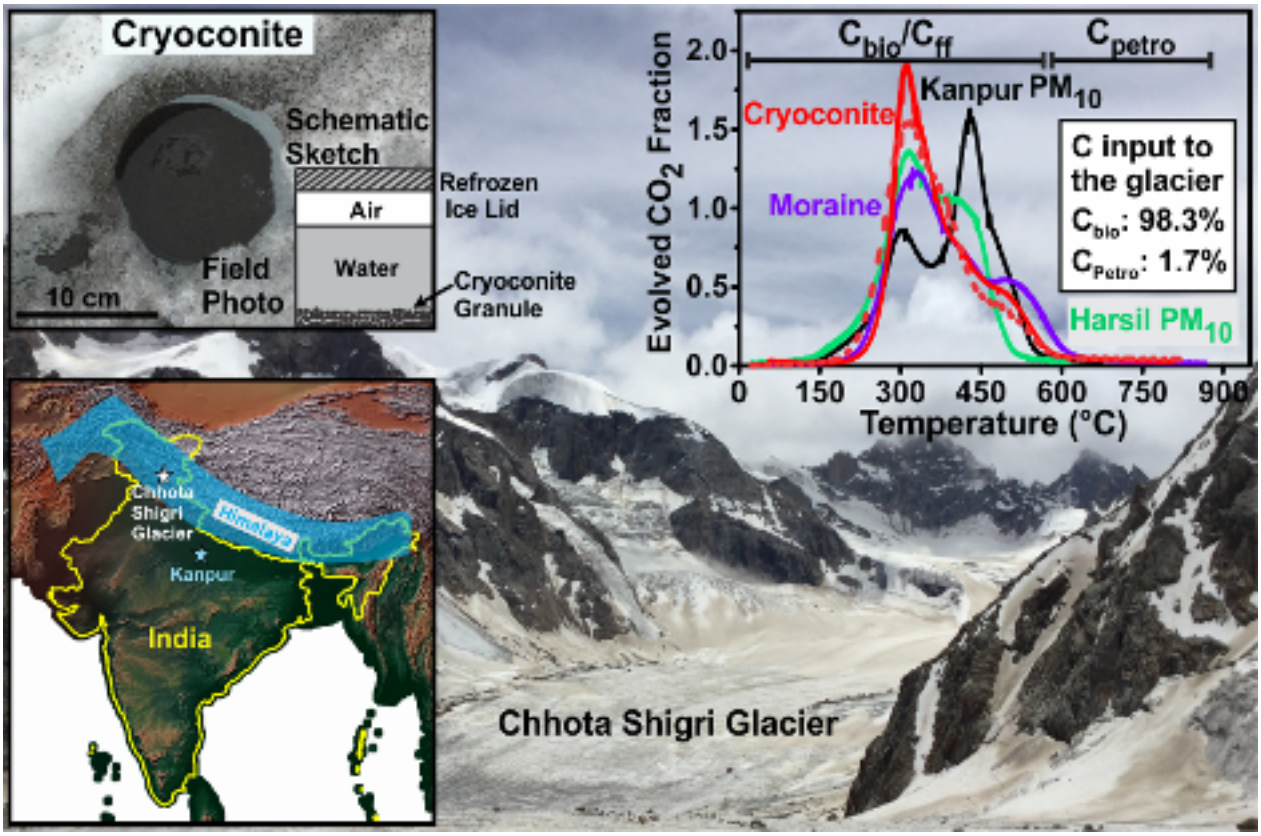
Cryoconite
Schematic Sketch
Refrozen Ice Lid
Air
Water
Cryoconite Granule
10 cm
Field Photo
Chhota Shigri Glacier
Kanpur
India
Himalaya
Evolved CO_2 Fraction
C_{bio}/C_{ff}
C_{petro}
Kanpur PM_{10}
Cryoconite
Moraine
Harsil PM_{10}
C input to the glacier
C_{bio}: 98.3%
C_{Petro}: 1.7%
Temperature (°C)
Chhota Shigri Glacier

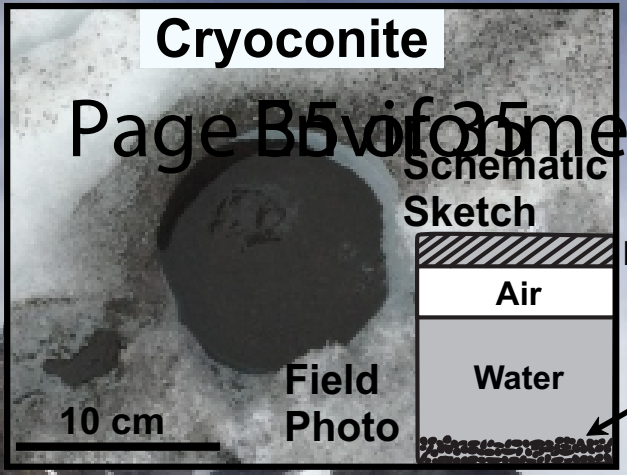

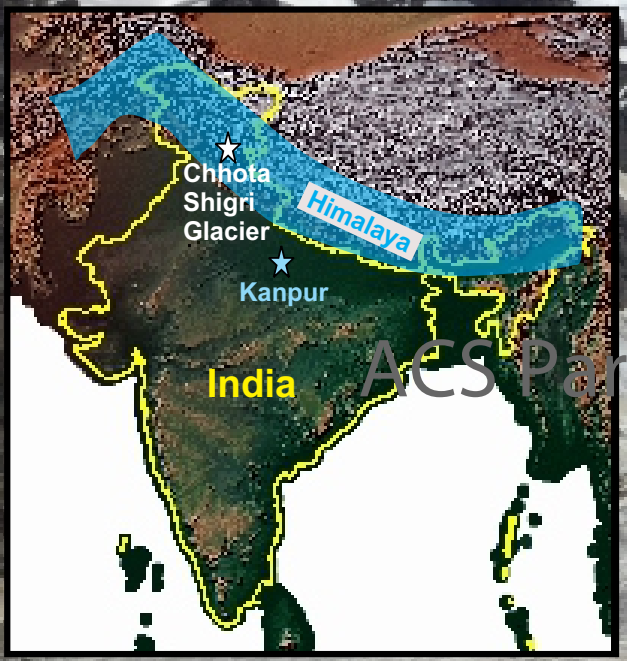

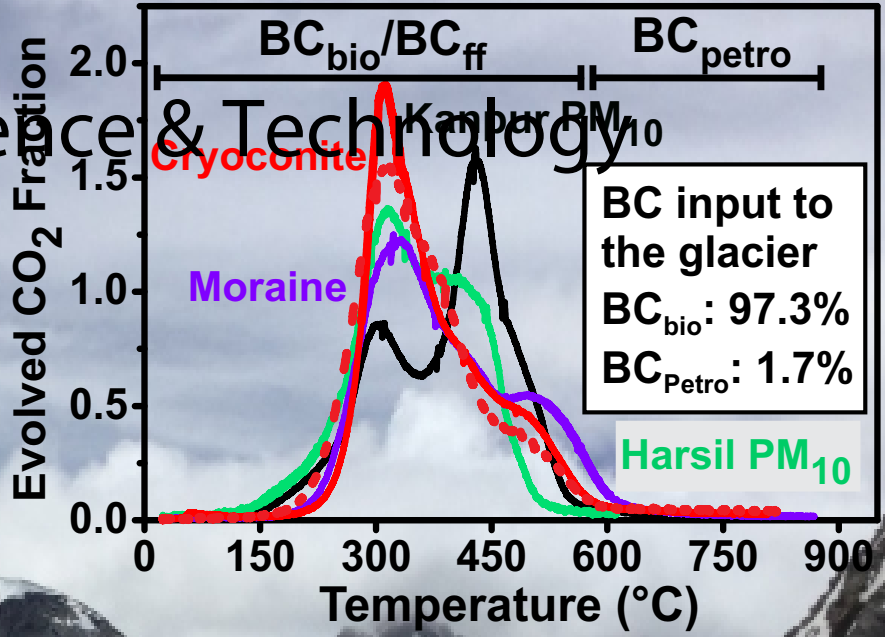

Chhota Shigri Glacier